

Processes associated with extremely heavy precipitation in the Meghalaya Plateau region: A case modelling study

Tanvir Ahmed^{1,2} | Joohyun Lee¹ | Han-Gyul Jin¹  | Jong-Jin Baik¹ 

¹School of Earth and Environmental Sciences, Seoul National University, Seoul, South Korea

²Department of Physics, Shahjalal University of Science and Technology, Sylhet, Bangladesh

Correspondence

J.-J. Baik, School of Earth and Environmental Sciences, Seoul National University, Seoul 08826, South Korea.
Email: jjbaik@snu.ac.kr

Funding information

National Research Foundation of Korea, Grant/Award Number:
NRF-2019R1A6A1A10073437

Abstract

The Meghalaya Plateau (MP) located in northeast India is one of the雨iest regions in the world. On 18–19 August 2015, Mawsynram on the southern slope of MP received 745 mm of precipitation in 24 hr. This study investigates the dynamical, thermodynamical and cloud microphysical processes associated with this event through numerical simulations with fine horizontal resolutions (1 and 1/3 km). The control (CNTL) simulation with 1 km grid spacing successfully reproduces the observed spatial pattern of accumulated precipitation. A simulation without MP (noMP) is carried out to examine the role of MP in this precipitation. From 1500 LST 18 to 0000 LST 19 (P1) when the low-level jet carrying warm and moist air towards MP is relatively weak, the upslope region receives a moderate amount of precipitation which is initiated over this region due to the orographic lifting, while almost no precipitation is received there in the noMP simulation. Warm microphysical processes play dominant roles in the precipitation in P1. From 0000 to 0900 LST 19 (P2) when the low-level jet is enhanced, the CNTL simulation shows very heavy precipitation in the upslope region, much heavier than that in the noMP simulation. Deep convective systems developed upwind of MP move towards MP. These convective systems merge together and strengthen over the upslope region. The accretion process is substantially enhanced by the vigorous updraughts at low levels over the steep slope of MP, resulting in heavy precipitation. The 1/3 km resolution simulation shows much heavier precipitation in the upslope region than the CNTL simulation. The increased horizontal resolution makes the slopes steeper, resulting in further intensification of the updraughts over this region. This increase in simulated precipitation reduces the deviation from the rain-gauge observation, implying the importance of very high horizontal resolutions in simulating extremely heavy precipitation in MP.

KEY WORDS

cloud microphysical process, extreme precipitation, Meghalaya Plateau, nocturnal low-level jet, orographic precipitation, WRF model

1 | INTRODUCTION

The Meghalaya Plateau (MP), located in northeast India and bordered to the south by Bangladesh, is one of the雨iest regions in the world. MP is oriented in the east–west direction, and its southern slope is made up of undulating hills and deep valleys responsible for the unique topographic features of the plateau. When the humid monsoonal wind blows from the Bay of Bengal, MP acts as an orographic barrier in its way to the Himalayas. Cherrapunji and Mawsynram, towns located atop steep cliffs in southern MP, receive average annual precipitation of $\sim 12,000$ and $\sim 12,600$ mm, respectively (Kuttippurath *et al.*, 2021). Most of the heavy precipitation events in MP occur during the active spells of the South Asian summer monsoon which has submonthly-scale intraseasonal oscillations (Fujinami *et al.*, 2011; Murata *et al.*, 2017). The rainwater runs off via streams and the Surma River to the lowland area of the Sylhet district of Bangladesh and generates flash floods that cause considerable loss of life and property in this region (Ohsawa *et al.*, 2001; Habib *et al.*, 2019).

The heavy rainfall in MP has attracted much scientific attention. Using daily rainfall data from 15 stations during 32 years (1975–2006), Goswami *et al.* (2010) showed that the heavy rainfall events ($>150 \text{ mm}\cdot\text{day}^{-1}$) in northeast India mainly occur during the peak monsoon season (June–August). The amount of monsoonal rainfall in northeast India has decreased in recent decades, but the decrease is a part of interdecadal oscillation which was found to be associated with the Pacific decadal oscillation (Choudhury *et al.*, 2019). Rather, northeast India experienced a significant increase in the number of extremely heavy rainfall events during the years 2000–2015 (Varikoden and Revadekar, 2020). By examining the lengths and phases of rainy spells, it was shown that the most extreme events are associated with either mesoscale, synoptic or large-scale systems rather than isolated thunderstorms. The observed rainfall in MP during the monsoon season shows the quasi-biweekly intraseasonal (7–25 days) variability (Murata *et al.*, 2008; Sato, 2013; Fujinami *et al.*, 2017). Murata *et al.* (2017) showed that the active rainfall spells at Cherrapunji start when anomalous anticyclonic circulation at 850 hPa propagating westward stays over the northern part of the Bay of Bengal. The westerlies in the northern part of the anomalous anticyclonic circulation enhance the moisture supply from the Bay of Bengal and the moisture convergence in northeast India, producing heavy rainfall over MP. In northeastern Bangladesh located in the vicinity of MP, the maximum rainfall is usually observed in the late night to early morning (Ohsawa *et al.*, 2001; Islam *et al.*, 2005; Terao *et al.*, 2006; Ahmed *et al.*, 2020a). Using 6-hourly rawinsonde data, Terao

et al. (2006) showed that the meridional wind speed is maximum at 0000 LST and the wind direction changes in the clockwise direction with height, indicating the existence of a nocturnal low-level jet (LLJ). They suggested that the nocturnal LLJ is a possible cause for the rainfall peak in the late night to early morning.

Compared to the observational studies, only a few numerical studies have been conducted to understand the characteristics and mechanisms of precipitation in MP. Kataoka and Satomura (2005) showed that the diurnal variation of precipitation, especially the maximum in the late night to early morning, is closely associated with the deep convective activity index derived from 3-hourly satellite data and that severe precipitation systems are triggered when strong southwesterlies with high equivalent potential temperature climb MP or a thick cold pool. Sato (2013) showed that the sufficient intensity and proper direction (southerly/southwesterly) of LLJ are needed to initiate orographic convection.

These previous numerical studies mainly focused on dynamical and thermodynamical processes. Orr *et al.* (2017) demonstrated the importance of cloud microphysical processes in the monsoonal precipitation in the central Nepalese Himalayas through numerical simulations using different cloud microphysics schemes. However, for precipitation in the MP region, cloud microphysical processes and their interactions with dynamical and thermodynamical processes have not been investigated in depth. This study aims to examine the cloud microphysical, dynamical and thermodynamical processes of extremely heavy precipitation in MP and their interactions. This study also aims to examine the effects of the complex topography within the plateau through numerical simulations using fine horizontal resolutions. The horizontal resolutions used in previous numerical studies (2–3.6 km) may not be sufficient to resolve the complex topography such as steep slopes and deep narrow valleys.

This article is organized as follows. The case description and the simulation set-up are presented in Section 2. Section 3 is dedicated to the simulation results and discussion. In Section 4, a summary and conclusions are given.

2 | CASE DESCRIPTION AND SIMULATION SET-UP

2.1 | Case description

A monsoonal heavy precipitation event occurred over and around MP on 18–19 August 2015. The maximum observed 24 hr accumulated precipitation amount during

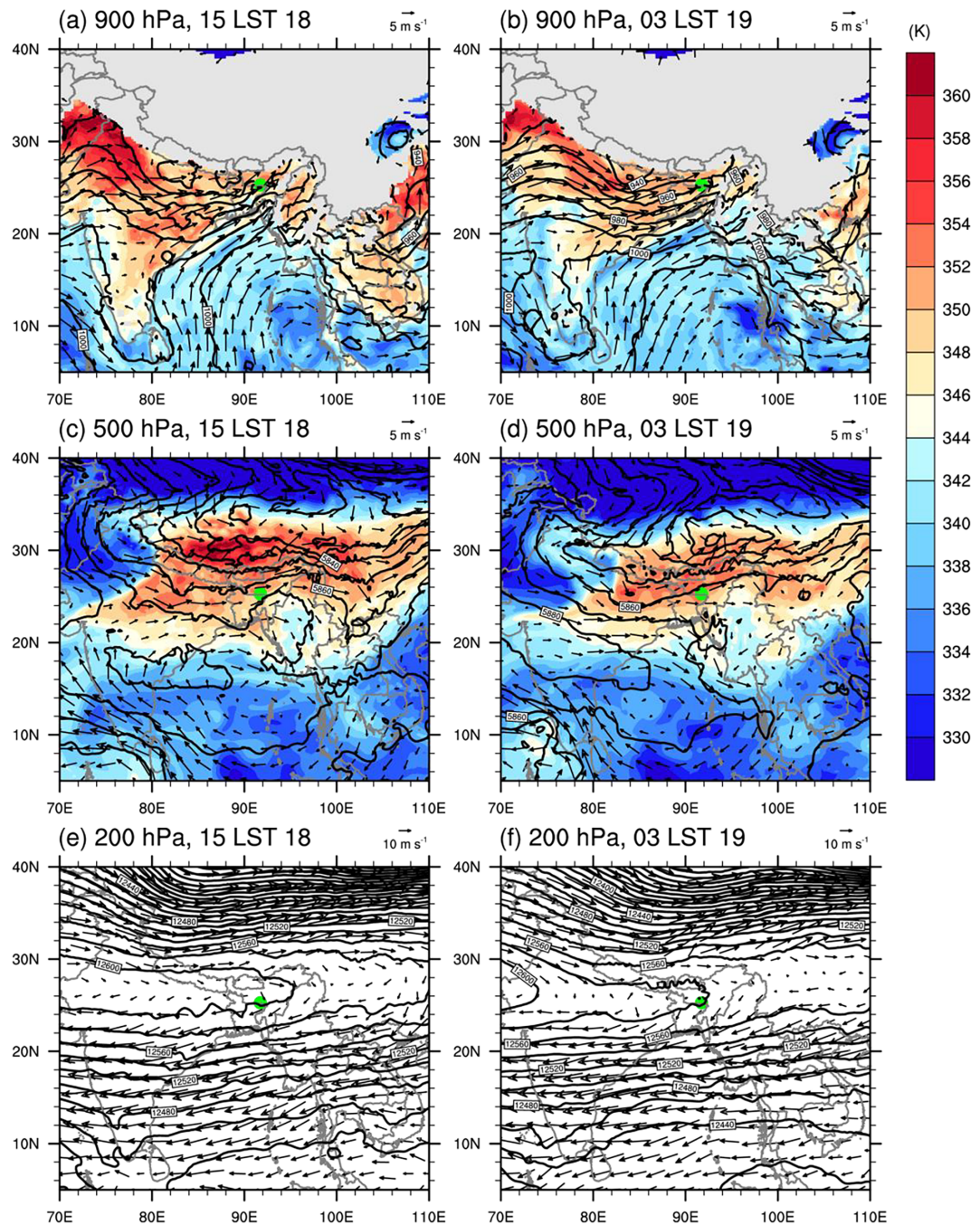


FIGURE 1 Geopotential height (m, black solid lines) and horizontal wind vector (arrows) fields at (a,b) 900 hPa, (c,d) 500 hPa and (e,f) 200 hPa, at (a,c,e) 1500 LST 18 and (b,d,f) 0300 LST 19 August 2015, from the ERA5 reanalysis data. Equivalent potential temperature (shaded) field is overlaid on the plots for 900 and 500 hPa. The green dot denotes Cherrapunji [Colour figure can be viewed at wileyonlinelibrary.com]

0300 UTC 18–0300 UTC 19 August 2015 was 745 mm at Mawsynram station. To examine the synoptic condition during this event, the ERA5 reanalysis data (Hersbach *et al.*, 2020) are used. Figure 1 shows the synoptic fields at 900, 500 and 200 hPa at 0900 and 2100 UTC 18 August 2015. At 0900 UTC 18, a monsoonal trough exists in the northeastern part of India and an anticyclonic circulation is centred at the southeastern part of the Bay of Bengal at the 900 hPa level (Figure 1a). The resultant southwesterly

flow transports the warm and moist air along the east coast of India towards the inland area of Bangladesh and MP. After 12 hr, the monsoonal trough moves eastward and the anticyclonic circulation over the Bay of Bengal moves westward, resulting in the enhancement of the southwesterly flow between them (Figure 1b). The inland area of Bangladesh exhibits higher equivalent potential temperature than 12 hr prior, which indicates the abundant supply of warm and moist air to MP at low levels. At

500 hPa, however, the westerly flow over and around MP is relatively weak compared to the southwesterly flow at 900 hPa (Figure 1c,d). At upper levels, divergence covers the Indo-Gangetic Plain and MP, which can be associated with active convection (Figure 1e,f). Northeasterlies blow over the south of MP at upper levels, in contrast with the southwesterlies at low levels. Directly over MP, upper-level northwesterlies appear at 0900 UTC 18 but they become very weak at 2100 UTC 18 when MP receives heavy nocturnal precipitation.

2.2 | Model description and simulation design

To simulate this heavy precipitation event, the Weather Research and Forecasting (WRF) model version 4.2 (Skamarock *et al.*, 2019) is used. For the initial and boundary conditions, the ERA5 reanalysis data (Hersbach *et al.*, 2020) with 0.25° horizontal resolution and 1 hr temporal resolution are used. The WRF model is integrated over 36 hr from 2100 UTC 17 (0300 LST 18) August 2015, and the simulation data from 0900 UTC 18 (1500 LST 18) to 0900 UTC 19 (1500 LST 19) August 2015 are used for analysis, to take into account the model spin-up time.

The main analysis area in this study includes regions with different local standard times, that is, MP in northeast India (UTC + 5 hr 30 min) and the upwind region of MP in Bangladesh (UTC + 6 hr). Hereafter, the local standard time of Bangladesh is used for the whole analysis area, regardless of the actual local standard time.

The model domain configuration is presented in Figure 2. In this study, three simulations are performed. The control (CNTL) simulation and the simulation without MP (noMP) use four nested domains from domains 1 to 4. The horizontal grid spacings of domains 1, 2, 3 and 4 are 27 km (181×166 grid points), 9 km (271×271), 3 km (331×376) and 1 km (481×421), respectively. For all domains, 42 vertical layers, which are stretched with height, are used. The time steps for domains 1, 2, 3 and 4 are 20, 6.66, 2.22 and 0.74 s, respectively. The terrain height of domain 4 presented in Figure 3 clearly shows the difference between the CNTL and noMP simulations. The terrain height of MP in the noMP simulation is reduced to 13 m which is the average height of the upwind region. This flattening process is applied to all domains, but with a relaxation process near the lateral boundaries in order to avoid abrupt changes in terrain height. The relaxation zone lies within ~20 km from the lateral boundaries, with a greater decrease in terrain height according to

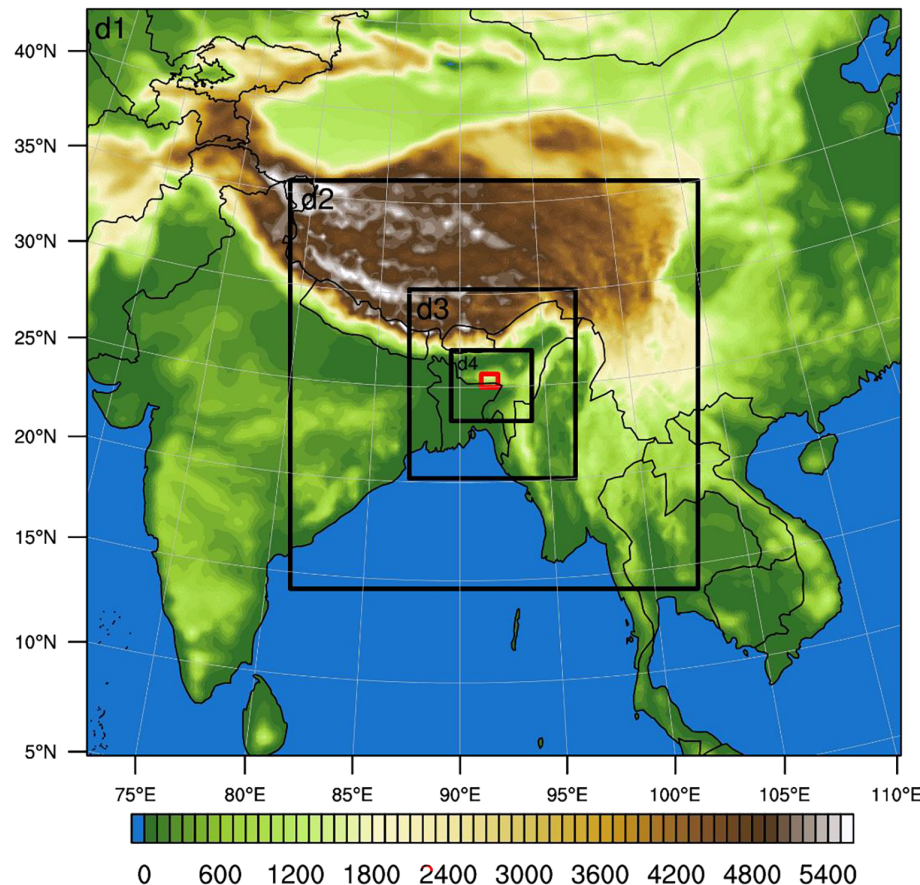


FIGURE 2 Four nested domains in the CNTL and noMP simulations and one additional domain in the HRES simulation with terrain height (m, shaded). d1, d2, d3 and d4 indicate domains 1, 2, 3 and 4, respectively. Domain 5 of the HRES simulation is indicated by the red box [Colour figure can be viewed at wileyonlinelibrary.com]

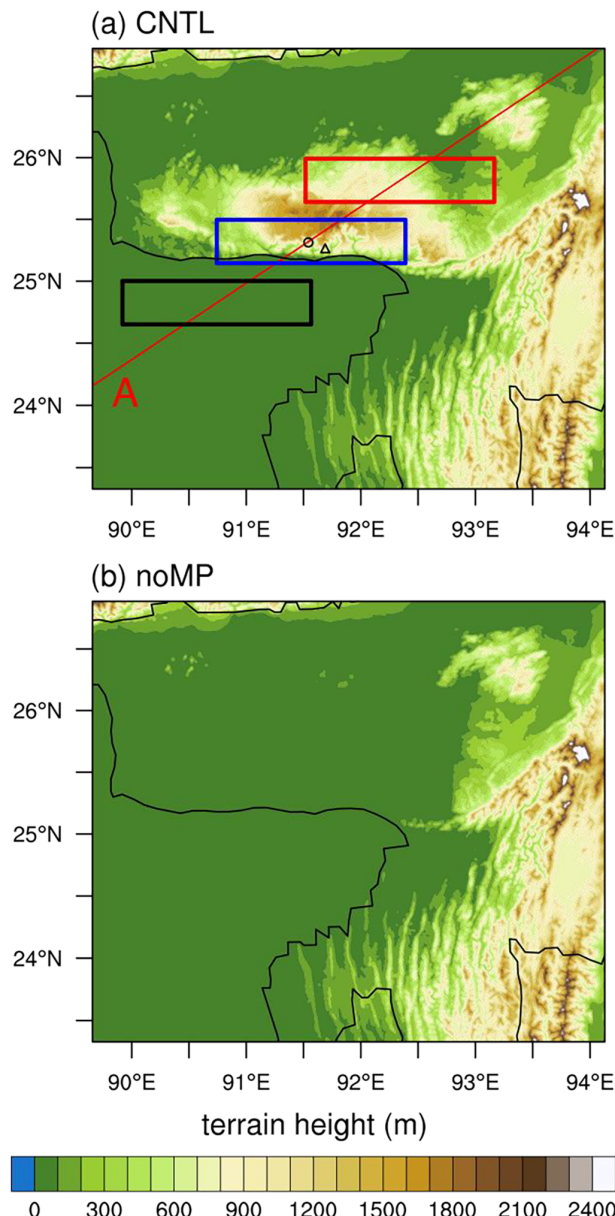


FIGURE 3 Terrain height in the innermost domain (domain 4) of the (a) CNTL and (b) noMP simulations. Black, blue and red boxes represent the upwind, upslope and downwind regions, respectively. Black hollow circle and triangle indicate Mawsynram (25.30°N , 91.58°E) and Cherrapunji (25.25°N , 91.73°E), respectively. Red line (Line A) represents the reference line used for analysis [Colour figure can be viewed at wileyonlinelibrary.com]

the distance from boundaries. The purpose of the noMP simulation is to find out the role of the steep southern slope of MP in the extremely heavy precipitation there. The comparison between the CNTL and noMP simulations is expected to reveal how much of the precipitation amount can be attributed to the presence of MP and how MP modulates the development and movement of convective systems. Figure 3a also shows a reference line (red line, Line A hereafter) that passes through Mawsynram

(black circle) and the upwind, upslope and downwind regions (black, blue and red boxes, respectively) that are determined based on the low-level wind direction and the movement of precipitation systems in this event.

A simulation with a higher horizontal resolution (HRES) than the CNTL simulation is performed to examine the effects of local topography on the heavy precipitation, focusing on the southern slope of MP. In the HRES simulation, one more nested domain with a horizontal grid spacing of $1/3\text{ km}$ is added as domain 5 (red box in Figure 2). Domain 5 consists of 301×241 grid points, and the time step is 0.25 s .

The physical parametrization schemes chosen for the simulations in this study are as follows: the Yonsei University (YSU) planetary boundary-layer scheme (Hong *et al.*, 2006), the Dudhia short-wave radiation scheme (Dudhia, 1989), the Rapid Radiative Transfer Model (RRTM) long-wave radiation scheme (Mlawer *et al.*, 1997), the unified Noah land surface model (Tewari *et al.*, 2004), and the Kain–Fritsch cumulus parametrization scheme (Kain, 2004). The cumulus parametrization scheme is not applied to domains 3, 4 and 5. The Thompson–Eidhamer cloud microphysics scheme (Thompson and Eidhamer, 2014) is used with the cloud droplet autoconversion and raindrop–cloud droplet accretion parametrizations replaced by those of Lee and Baik (2017) and Ahmed *et al.* (2020b), respectively.

3 | RESULTS AND DISCUSSION

3.1 | Validation and precipitation characteristics

The numerical simulation of this event successfully reproduces the observed spatial distribution of accumulated precipitation. Figure 4 shows the comparison of 24 hr (0900 LST 18–0900 LST 19 August 2015) accumulated precipitation amount in the CNTL simulation and the rain-gauge observation. The rain-gauge data in Bangladesh are 3-hourly and were provided by the Bangladesh Meteorological Department. The rain-gauge data in India are daily, starting from 0300 UTC every day, and were provided by the India Meteorological Department. The observed spatial pattern of precipitation that shows the largest amount of accumulated precipitation on the southern slope of MP and relatively small amount of accumulated precipitation in the other parts of MP is reproduced in the CNTL simulation (Figure 4a). The simulated precipitation southwest of MP, however, cannot be properly evaluated because of the lack of rain-gauge stations in this region of Bangladesh. The amounts of accumulated precipitation at Cherrapunji and

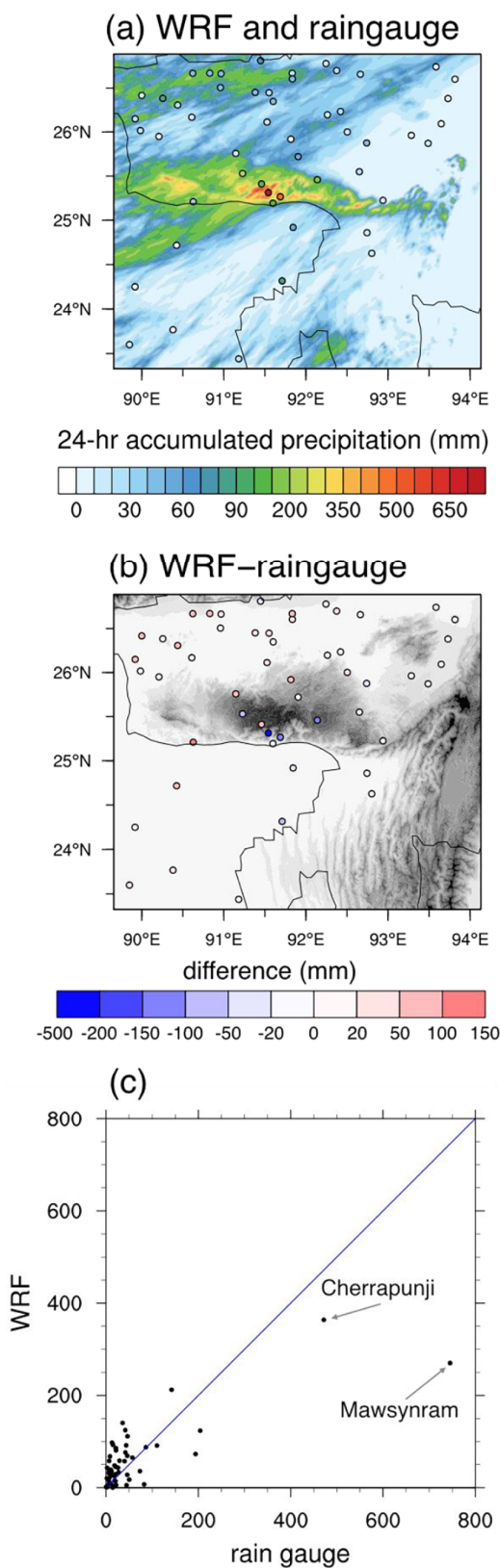


FIGURE 4 (a) Twenty-four hour accumulated precipitation amount from the rain-gauge observation (circles) and the CNTL simulation (shaded), and (b) their difference. (c) Scatter plot of the rain-gauge observation and CNTL simulation for the 24 hr accumulated precipitation amount (mm) [Colour figure can be viewed at wileyonlinelibrary.com]

Mawsynram, the two stations that experienced the most extreme precipitation, are underestimated by 108 and 475 mm, respectively. The deviation of simulated precipitation amount from the observation at these stations are largely reduced in the HRES simulation that better resolves the local topography, which will be shown in Section 3.4. The correlation coefficient between the observed and simulated 24 hr accumulated precipitation amounts is 0.78, which is high enough to assume that the simulations of this event in this study are valid.

To examine the temporal evolution of precipitation, the time series of precipitation rate over the upwind, upslope and downwind regions in the CNTL and noMP simulations are presented in Figure 5. In the upwind region (Figure 5a), the precipitation rate in the CNTL simulation is very small until 2210 LST 18 ($0.8 \text{ mm}\cdot\text{hr}^{-1}$ on average) and then it increases abruptly and reaches its peak at 0050 LST 19 ($10.1 \text{ mm}\cdot\text{hr}^{-1}$). In this region, the CNTL and noMP simulations show similar time series of precipitation rate until ~ 0300 LST 19, and then the precipitation rate in the noMP simulation sharply decreases while that in the CNTL simulation shows a relatively delayed decrease. In the upslope region, the CNTL simulation shows moderate precipitation rates ($4.2 \text{ mm}\cdot\text{hr}^{-1}$ on average) until 0030 LST 19 when the precipitation rate starts to increase rapidly. This, together with the fact that the upwind region receives only a little precipitation in the afternoon and evening, means that the precipitation systems are newly developed over the upslope region. The start of the rapid increase in precipitation rate is delayed by 2 hr 20 min in the upslope region, and this increase corresponds to the arrival of the precipitation systems that were pre-developed upwind of MP. The peak value in the upslope region in the CNTL simulation ($20.3 \text{ mm}\cdot\text{hr}^{-1}$) is more than twice that in the noMP simulation ($8.7 \text{ mm}\cdot\text{hr}^{-1}$), indicating that the advected precipitation systems are further intensified over the southern slope of MP. The precipitation rate in the upslope region in the CNTL simulation shows another abrupt increase from 0530 LST 19, which does not appear in the noMP simulation. In the downwind region (Figure 5c), the overall precipitation rate is relatively small in both simulations.

From the time series of precipitation rate, it is shown that the roles of MP in precipitation are to initiate or enhance it in the upslope region and to prolong the precipitation in the upwind region. The enhancement of precipitation by orography in South Asia has been reported in many studies where numerical model simulations with and without some orography within South Asia were carried out (Wang and Chang, 2012; Wu *et al.*, 2014). Wu *et al.* (2014) showed that the Arakan Mountains anchor and enhance precipitation in this region during the onset of monsoon and also affect large-scale circulations. MP

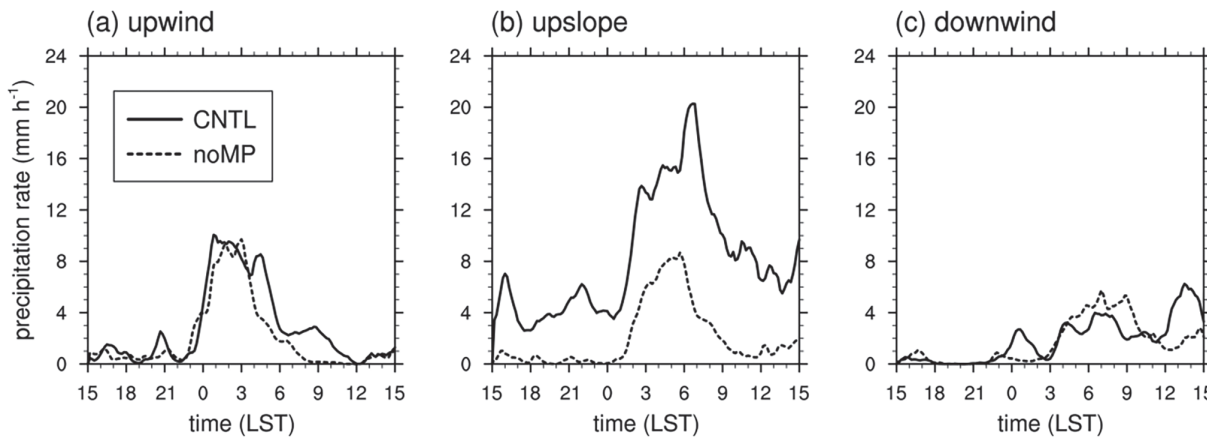


FIGURE 5 Time series of area-averaged precipitation rate for the (a) upwind, (b) upslope and (c) downwind regions, in the CNTL (solid) and noMP (dashed) simulations

may also have some effects on large-scale circulations, which deserves investigation in a future work.

The analysis period in this study is divided into two phases: before/after the abrupt increase in precipitation rate. The 9 hr accumulated precipitation amount and 900 hPa wind fields of Phase 1 (1500 LST 18–0000 LST 19, P1 hereafter) and Phase 2 (0000–0900 LST 19, P2 hereafter) are shown in Figure 6. P1 shows concentrated precipitation on the southern slope of MP where the prevailing southwesterlies go through orographic lifting. In contrast, there is only a little precipitation upwind of MP in this period. P2 shows a much larger amount of precipitation on the southern slope of MP and stronger southwesterlies compared to P1. In P2, some areas upwind of MP receive a considerable amount of precipitation and they are elongated in the low-level wind direction, indicating the path of the pre-developed precipitation systems towards MP.

From the above results, P1 can be characterized by the period when the precipitation is initiated by MP, while P2 can be characterized by the period when the precipitation is intensified over the southern slope of MP. In the upslope region, 75% of the total accumulated precipitation amount in the upslope region occurs in P2, implying that the intensification process may contribute more to the accumulated precipitation amount than the initiation process does.

3.2 | Dynamical and thermodynamical characteristics

In this subsection, the dynamical and thermodynamical processes associated with this extreme precipitation case are examined. The development of the nocturnal LLJ heading towards MP has been attributed to the heavy precipitation in this region in many previous studies (e.g.

Terao *et al.*, 2006; Sato, 2013). Figure 7 shows the evolution of the vertical profiles of horizontal wind speed along the direction of Line A and equivalent potential temperature averaged over the upwind region. All wind profiles have peaks below $z = 1$ km (Figure 7a). This vertical maximum of low-level wind speed is 9.5 m s^{-1} at 1800 LST 18 and increases up to 17.3 m s^{-1} at 0600 LST 19, and then decreases. The acceleration of low-level winds in the late night indicates the nocturnal enhancement of LLJ, which is typically found in this region during the monsoon season (Terao *et al.*, 2006; Sato, 2013; Fujinami *et al.*, 2017; Ahmed *et al.*, 2020a).

The nocturnal LLJ is associated with synoptic forcing and the diurnal variation of convective instability. During this precipitation event, synoptic low-level southwesterlies towards MP blow between the trough over the northeastern part of India and the high pressure system over the Bay of Bengal (Figure 1a,b). In the daytime (1800 LST 18 and 1000 LST 19), the atmosphere below $z = 1$ km in the upwind region is conditionally unstable, while it is slightly stable or almost neutral in the nighttime and early morning (2200 LST 18, 0200 LST 19 and 0600 LST 19) (Figure 7b). Terao *et al.* (2006) suggested that LLJ is enhanced in the nighttime as daytime convection that exerts a considerable damping effect on the boundary-layer winds diminishes after sunset, which is widely known as an important mechanism for nocturnal the LLJ (Blackadar, 1957; Jiang *et al.*, 2007). In the upwind region, the nocturnal acceleration of winds is not limited in the boundary layer although the amplitude of the acceleration tends to decrease with height. As Terao *et al.* (2006) conjectured, the large vertical scale of daytime convection in this region, which is supported by the daytime conditional instability appearing up to 4 km (Figure 7b), may induce the deceleration of winds in the free atmosphere as well.

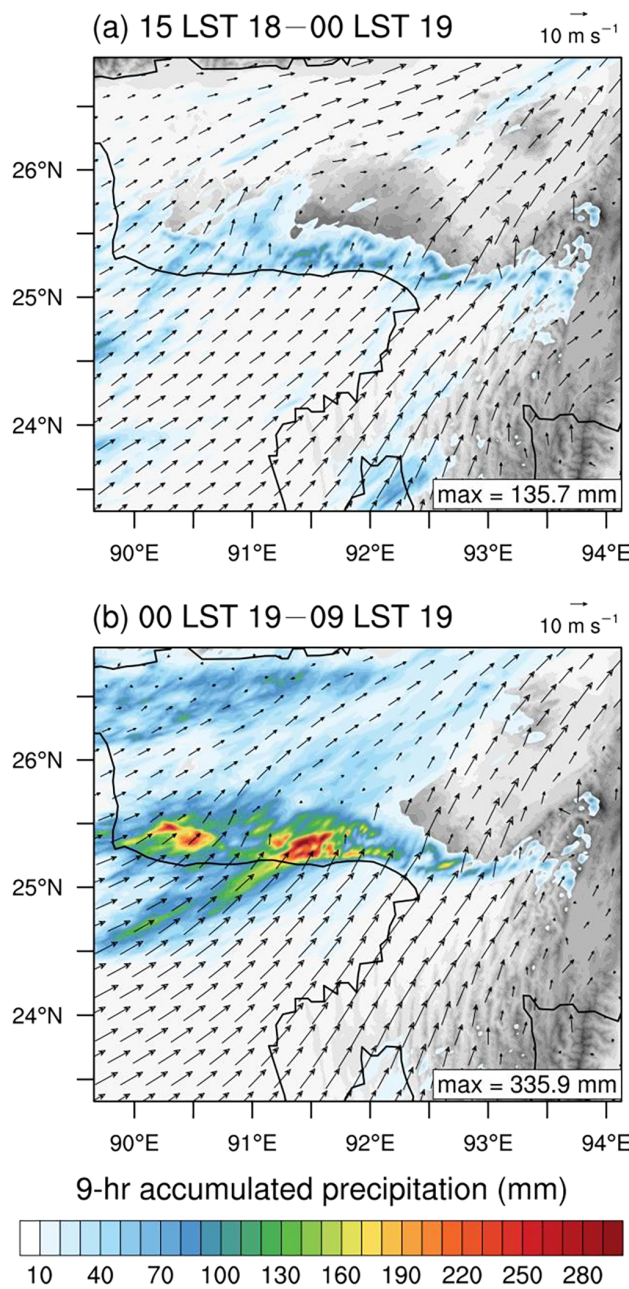


FIGURE 6 Nine-hour accumulated precipitation amount (shaded in colour) and 900 hPa level wind vector (arrows) fields with terrain height (shaded in black) during (a) 1500 LST 18–0000 LST 19 and (b) 0000–0900 LST 19 August 2015 [Colour figure can be viewed at wileyonlinelibrary.com]

Because the precipitation in MP is largely affected by the water vapour transported by LLJ, it is important to examine how much water vapour has been transported. Figure 8b shows the time series of water vapour flux along the direction of Line A at 900 hPa averaged over the upwind region. The time series of water vapour flux is similar to that of horizontal wind speed (Figure 8a). This indicates that the variability of water vapour flux is mainly modulated by the horizontal wind speed, not by

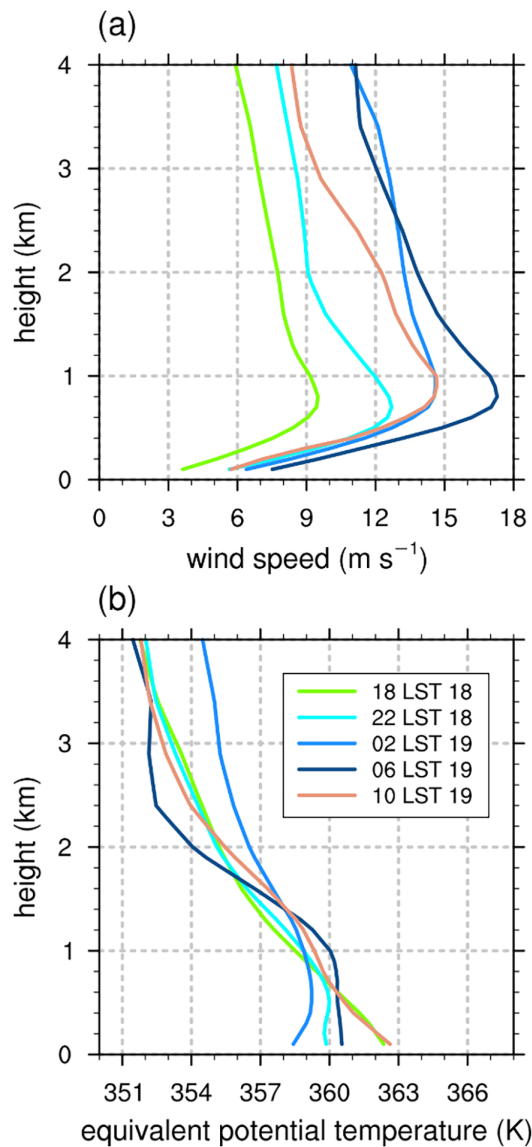


FIGURE 7 Vertical profiles of the area-averaged (a) wind speed component along the direction of Line A in Figure 3a and (b) equivalent potential temperature in the upwind region [Colour figure can be viewed at wileyonlinelibrary.com]

the mixing ratio of water vapour. The water vapour flux increases almost monotonically from 1640 LST 18 to 0530 LST 19. This increasing trend of water vapour flux is similar to the trend of precipitation rate in the upslope region (Figure 5b) with a 1 to 2 hr delay. This suggests that the water vapour flux over the upwind region is a main factor that affects the precipitation rate in the upslope region.

Figure 9 shows the vertical cross-sections of wind vector and water vapour flux at 1800 LST 18 and 0600 LST 19 along Line A (Figure 3a). At 1800 LST 18, the layer with water vapour flux (greater than $25 \text{ g kg}^{-1} \cdot \text{m s}^{-1}$) upwind of MP appears up to $z \sim 5 \text{ km}$. The water vapour flux upwind of MP is especially large at low levels ($z < 2 \text{ km}$), but it is small over the upslope of MP. At 0600 LST 19, the

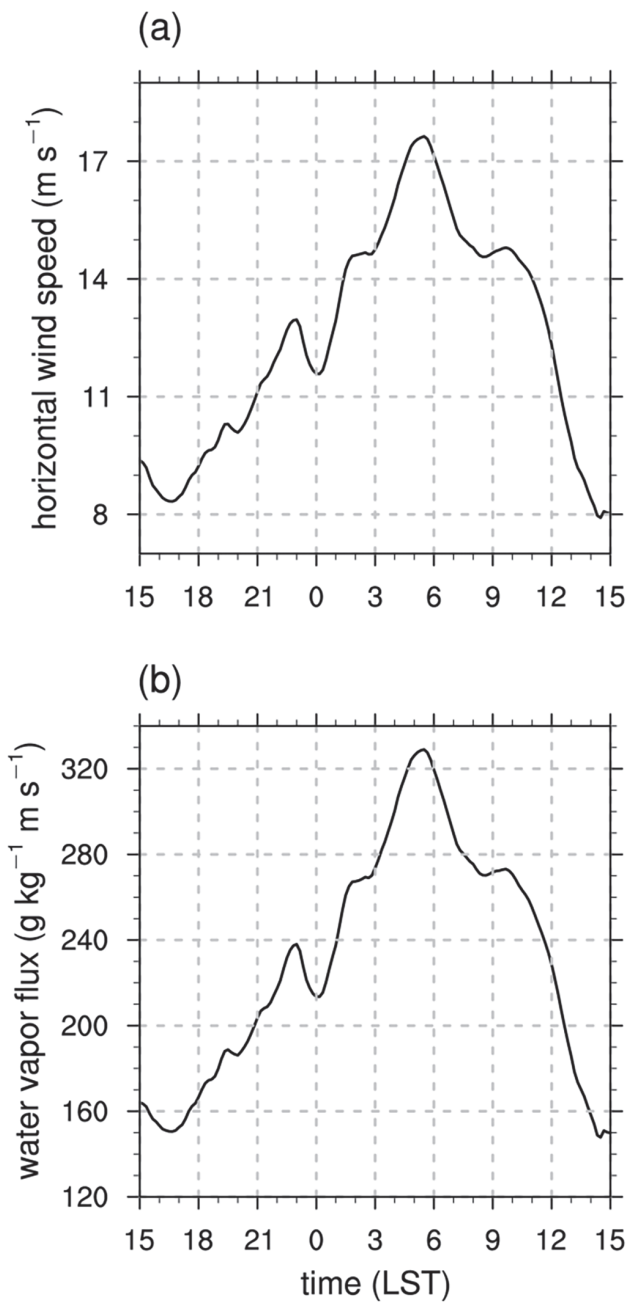


FIGURE 8 Time series of (a) horizontal wind speed and (b) water vapour flux at 900 hPa along the direction of Line A averaged over the upwind region

layer with water vapour flux (greater than $25 \text{ g}\cdot\text{kg}^{-1}\cdot\text{m}\cdot\text{s}^{-1}$) upwind of MP is thickened up to $z \sim 7 \text{ km}$, and the water vapour flux within $z < 2 \text{ km}$ is increased about 1.5 times due to strong LLJ. When this LLJ reaches the upslope of MP, it is deflected upward and strengthened to some extent (Figure 9b). As a result, a large amount of water vapour is transported upward. More water vapour can condense into cloud droplets releasing more latent heat, hence promoting deep convection. Another notable feature at this time is the upper-level wind direction. At 1800 LST 18, the winds

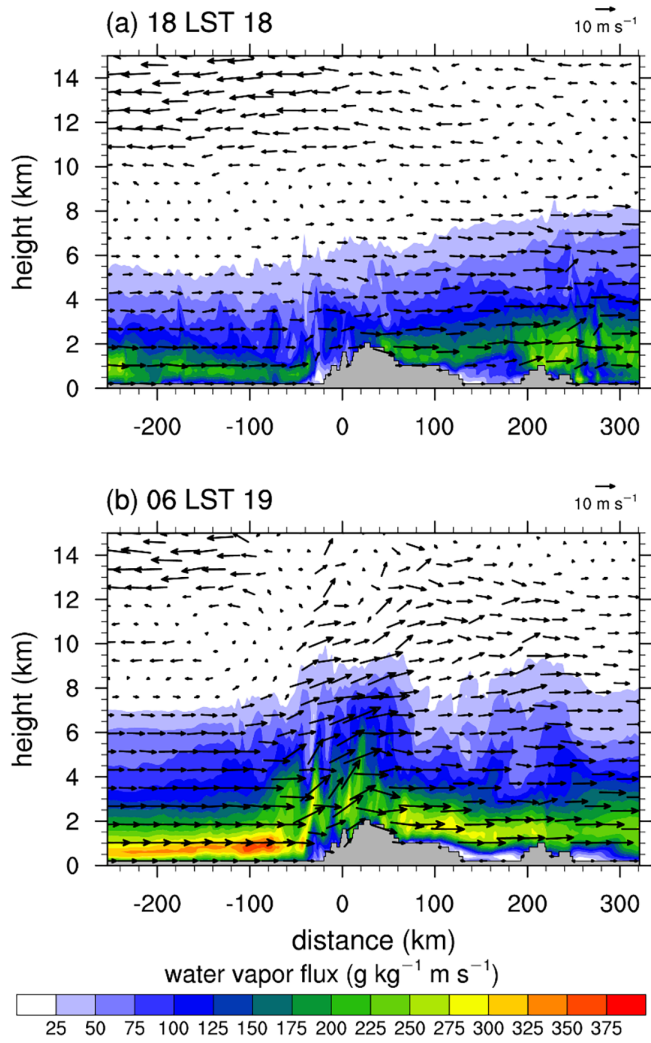


FIGURE 9 Vertical cross-sections of water vapour flux (shaded) and wind vector along Line A at (a) 1800 LST 18 and (b) 0600 LST 19 August 2015 [Colour figure can be viewed at wileyonlinelibrary.com]

at $z > \sim 10 \text{ km}$ over MP blow to the southwest, consistent with those upwind of MP. At 0600 LST 19, however, winds blow to the northeast at almost all levels over MP, forming divergence at $z > \sim 7 \text{ km}$ where the winds upwind of MP blow to the southwest or are relatively weak. It seems that the intensified LLJ rising over the steep upslope of MP makes a contribution to the change in the upper-level wind direction over MP.

Figure 10 shows the vertical cross-sections of vertical velocity. At 2100 LST 18 when the low-level jet is weak, shallow and weak updraughts appear over the upslope region (Figure 10a). At 0200 LST 19, deep and strong updraughts appear upwind of MP and approach MP (Figure 10b). The strong vertical wind shear upwind of MP shown in Figure 9 tilts the updraughts to the left (southwest). At 0600 LST 19, the updraughts approaching MP merge and become stronger over the upslope

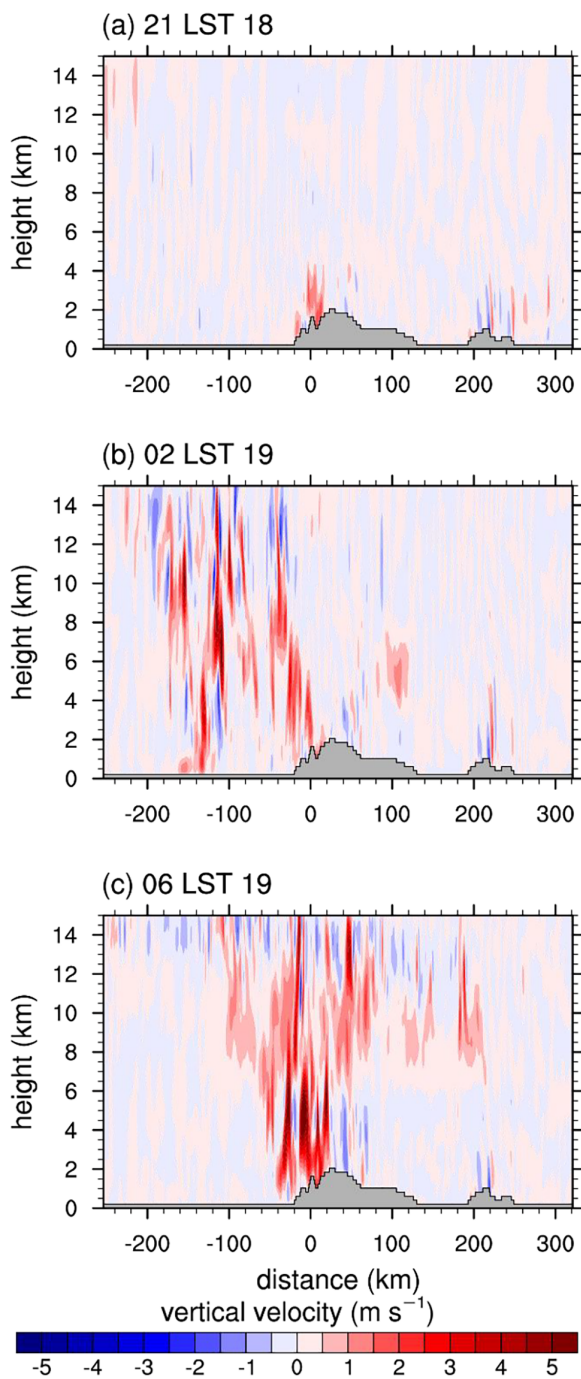


FIGURE 10 Vertical cross-sections of vertical velocity along Line A at (a) 2100 LST 18, (b) 0200 LST 19 and (c) 0600 LST 19 August 2015 [Colour figure can be viewed at wileyonlinelibrary.com]

region (Figure 10c). At this time, the updraughts develop relatively upright over the upslope region where the vertical wind shear is weak (Figure 9b). The horizontal scale of the merged system is larger than that of individual updraughts. The merged system is expanded to the right (northeast) at upper levels, mainly due to the upper-level divergence and resultant horizontal spread of upper-level clouds.

3.3 | Cloud microphysical characteristics

In this subsection, the cloud microphysical processes involved in this extreme precipitation case are examined. Figure 11 shows the time series of liquid water path (LWP) and ice water path (IWP) over the upwind, upslope and downwind regions in the CNTL and noMP simulations. Before ~0000 LST 19, in the upwind region, LWP and IWP are very small in both simulations. In the upslope region, LWP in the CNTL simulation is $\sim 1.5 \text{ kg} \cdot \text{m}^{-2}$ while that in the noMP simulation is still very small. Both simulations show very small IWP. These indicate that the moderate precipitation initiated in the upslope region in P1 is produced almost solely by warm microphysical processes. After ~0000 LST 19, in the upwind region, LWP and IWP increase abruptly in both simulations. Both warm and cold microphysical processes are involved in the precipitation systems in the upwind region. Unlike in P1, the cold microphysical processes contribute to the precipitation in P2. MP enhances both warm and cold microphysical processes. In the downwind region, due to the intense precipitation over in upslope region, LWP and IWP are relatively small.

For a detailed analysis of the cloud microphysical characteristics, vertical profiles of hydrometeors and microphysical conversion rates related to rainwater production averaged over the upslope region are presented in Figures 12 and 13, respectively. At 2100 LST 18, the cloud water, rainwater and snow are the main hydrometeors in the CNTL simulation, accounting for 25%, 56% and 19% of the total hydrometeor mixing ratio, respectively (Figure 12a). The cloud water and rainwater exist at $z < \sim 6 \text{ km}$, and their mixing ratios increase with decreasing height. In contrast, the snow appears at $z > \sim 6 \text{ km}$ and its mixing ratio peaks at $z \sim 10 \text{ km}$, leaving little chance of mixed-phase microphysical processes such as riming. In the noMP simulation, there are very small amounts of cloud water and rainwater, but snow exists at a similar amount as in the CNTL simulation (Figure 12b). The differences in cloud water and rainwater mixing ratios between the CNTL and noMP simulations increase with decreasing height (Figure 12c). These differences are mainly attributed to the accretion rate. The accretion rate is dominant and increases with decreasing height in the CNTL simulation, while the conversion processes rarely occur in the noMP simulation (Figure 13a,b). The active accretion process in P1 in the CNTL simulation is mainly attributed to the updraughts over the upslope region (Figure 10a) that supply a large amount of cloud droplets to be collected by raindrops. This accretion process acts as the key factor for the precipitation in the upslope region in P1.

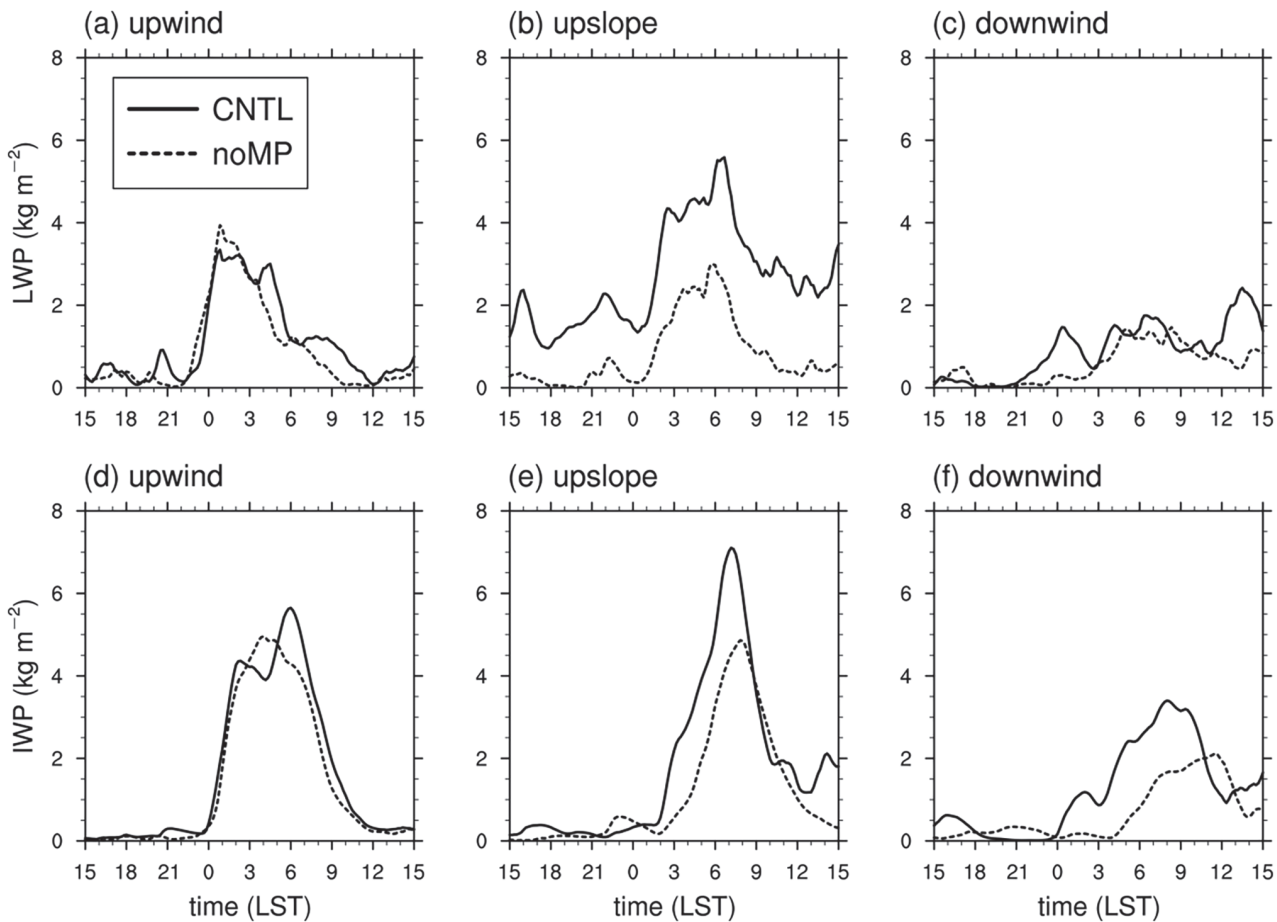


FIGURE 11 Time series of (a–c) LWP and (d–f) IWP averaged over the (a,d) upwind, (b,e) upslope and (c,f) downwind regions, in the CNTL (solid) and noMP (dashed) simulations

At 0600 LST 19, in the CNTL simulation, snow and rainwater mixing ratios increase substantially and a small amount of graupel appears at $z = \sim 4\text{--}8\text{ km}$ (Figure 12d). The noMP simulation also shows a large amount of hydrometeors (Figure 12e) because many of the precipitation systems are not generated over the upslope but previously developed upwind of MP and advected towards the upslope (Figure 5a). Compared to the noMP simulation, the CNTL simulation shows much larger snow and rainwater mixing ratios (Figure 12f). This indicates that the heavier precipitation in the CNTL simulation is caused by the enhancement of both warm and cold microphysical processes. The difference in vertical profiles of conversion rates shows that the accretion process and the melting process are more active in the CNTL simulation than in the noMP simulation (Figure 13f). The increment of accretion rate is much larger than that of melting rate. The larger vertical velocities in the merged and intensified updraughts over the upslope region as well as the enhanced melting of ice hydrometeors that produces raindrops enhance the accretion process. The increment of melting rate in the upslope region is relatively small

because a large amount of snow produced at upper levels is advected to upwind and downwind of MP due to the upper-level divergence. Therefore, the heavier precipitation in the CNTL simulation than in the noMP simulation in P2 is mainly attributed to the more active accretion process and partly attributed to the more active melting process.

Figure 14 shows the vertical cross-sections of liquid and ice hydrometeor mixing ratios. It is seen that the precipitation in the upslope region at 2100 LST 18 in P1 is produced almost solely by warm microphysical processes (Figure 14a). At 0200 LST 19, a number of deep convective systems with both liquid and ice hydrometeors are generated upwind of MP and move to the northeast in both CNTL and noMP simulations (Figure 14c,d). These convective systems slow down over the southern slope of MP and merge together as shown in the CNTL simulation at 0600 LST 19 (Figure 14e). The merged system includes the ice-phase clouds at upper levels going ahead. Due to the upper-level divergence, the ice hydrometeors at the upper level in the CNTL simulation are transported far to the northeast, which is not accompanied by

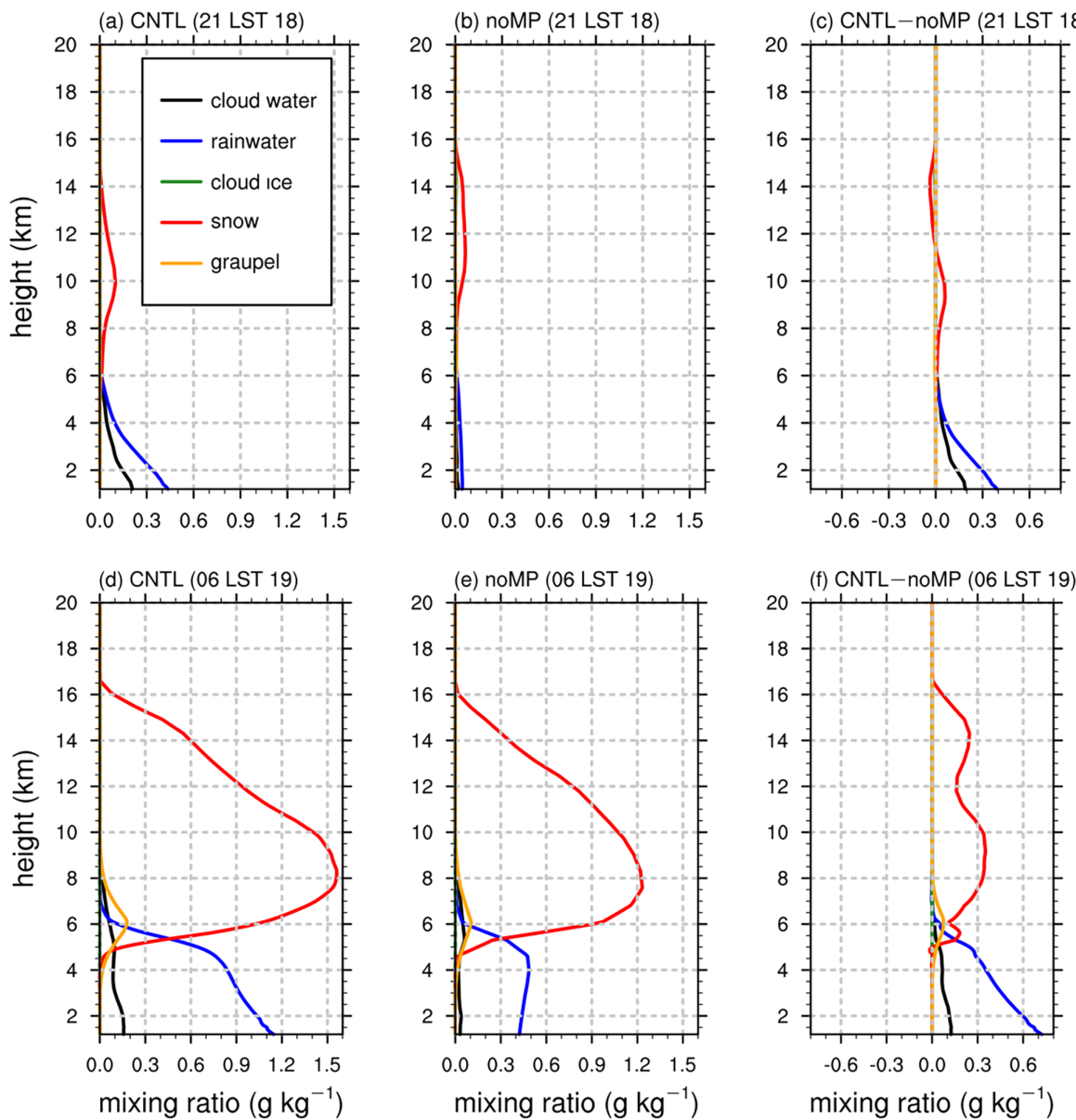


FIGURE 12 Vertical profiles of hydrometeor mixing ratios averaged over the upslope region at (a–c) 2100 LST 18 and (d–f) 0600 LST 19 August 2015 in the (a,d) CNTL and (b,e) noMP simulations, and (c,f) their differences. The hydrometeor that each line colour indicates is shown in (a) [Colour figure can be viewed at wileyonlinelibrary.com]

the liquid hydrometeors below. Because the noMP simulation does not show either the merging of convective systems or the upper-level clouds going ahead, the existence of MP is attributed to these features in the CNTL simulation.

3.4 | Local topographic effects on precipitation

Many valleys and ridges in the southern slope of MP create complex terrain with steep slopes (Figure 15a). The steep slopes are closely related to the formation of orographic

flows, which can be related to precipitation. In this subsection, by comparing the HRES simulation with the CNTL simulation, the effects of local topography on precipitation are investigated. The HRES simulation with the finer horizontal resolution better represents the local topography than the CNTL simulation. The difference in terrain height between the HRES and CNTL simulations (Figure 15b) shows that the effects of the increase in horizontal resolution are pronounced in the valley regions. The terrain height in the HRES simulation is lower inside the valleys and higher at the valley slope, which means that the slope of the HRES simulation is steeper than that of the CNTL simulation.

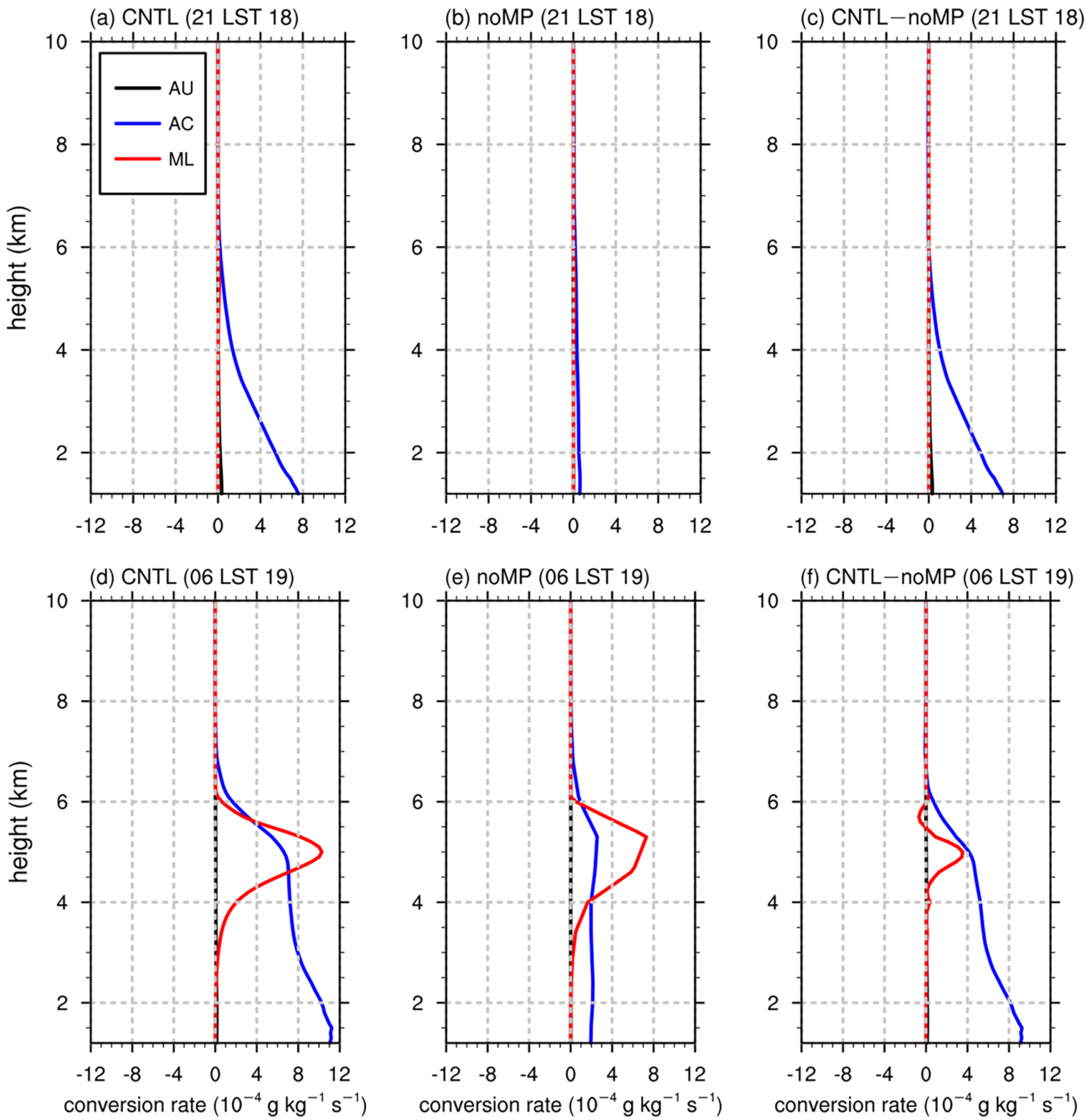


FIGURE 13 Vertical profiles of microphysical conversion rates related to rainwater production (AU: autoconversion, AC: accretion, ML: melting) averaged over the upslope region at (a–c) 2100 LST 18 and (d–f) 0600 LST 19 August 2015 in the (a,d) CNTL and (b,e) noMP simulations, and (c,f) their differences. The conversion rate that each line colour indicates is shown in (a) [Colour figure can be viewed at wileyonlinelibrary.com]

Note that the results in this subsection should be interpreted with caution because the differences in the results of the HRES and CNTL simulations are caused not only by the better representation of local topography but also by better resolving of physical processes due to the fine model resolution in the HRES simulation. Additional simulations may be needed to separate these two effects. Also, the effects of local topography are not wholly considered because the two simulations share the same

input topographical data with a 30 arc-second resolution, the Global Multi-resolution Terrain Elevation Data 2010 (Danielson and Gesch, 2011) developed by United States Geological Survey. The upper quartiles of magnitudes of positive and negative changes in topographical height from the CNTL simulation to the HRES simulation are both 25 m. These values increase by 75% and 76%, respectively, if the Shuttle Radar Topographic Mission data (Farr *et al.*, 2007) with a 3 arc-second resolution

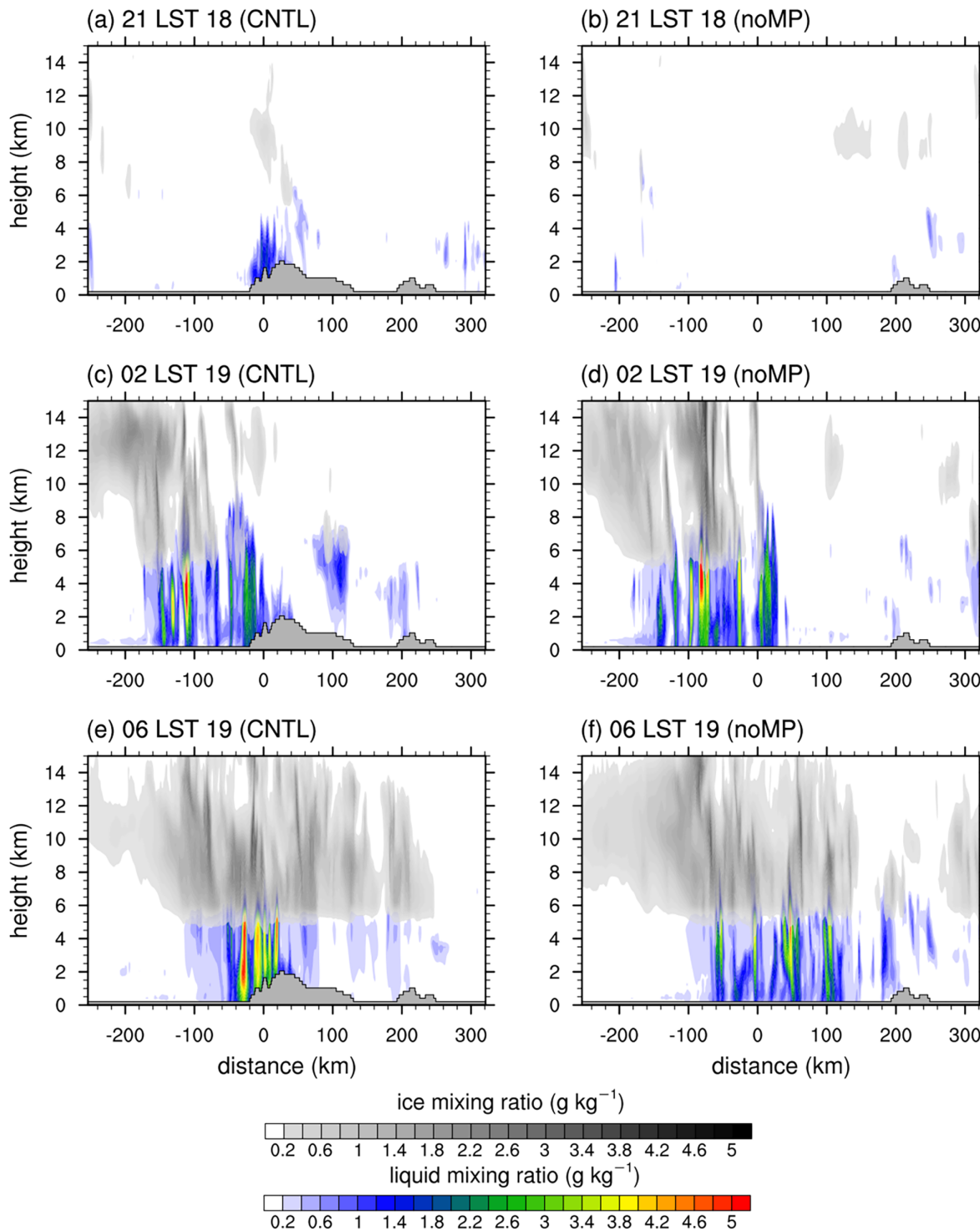


FIGURE 14 Vertical cross-sections of liquid and ice hydrometeor mixing ratios at (a,b) 2100 LST 18, (c,d) 0200 LST 19 and (e,f) 0600 LST 19 August 2015, in the (a,c,e) CNTL and (b,d,f) noMP simulations [Colour figure can be viewed at wileyonlinelibrary.com]

are used as the input topographical data in the HRES simulation.

The heavy precipitation is mainly simulated over the ridges branching out southward and the slopes near these ridges (Figure 15c). The 24 hr accumulated precipitation amount in the HRES simulation is overall

greater compared to that in the CNTL simulation except around the western region of Mawsynram (Figure 15d). This reduces the deviation of the simulated precipitation amount from the rain-gauge observation seen in the CNTL simulation. The 24 hr accumulated precipitation amounts in the rain-gauge observation, CNTL simulation and

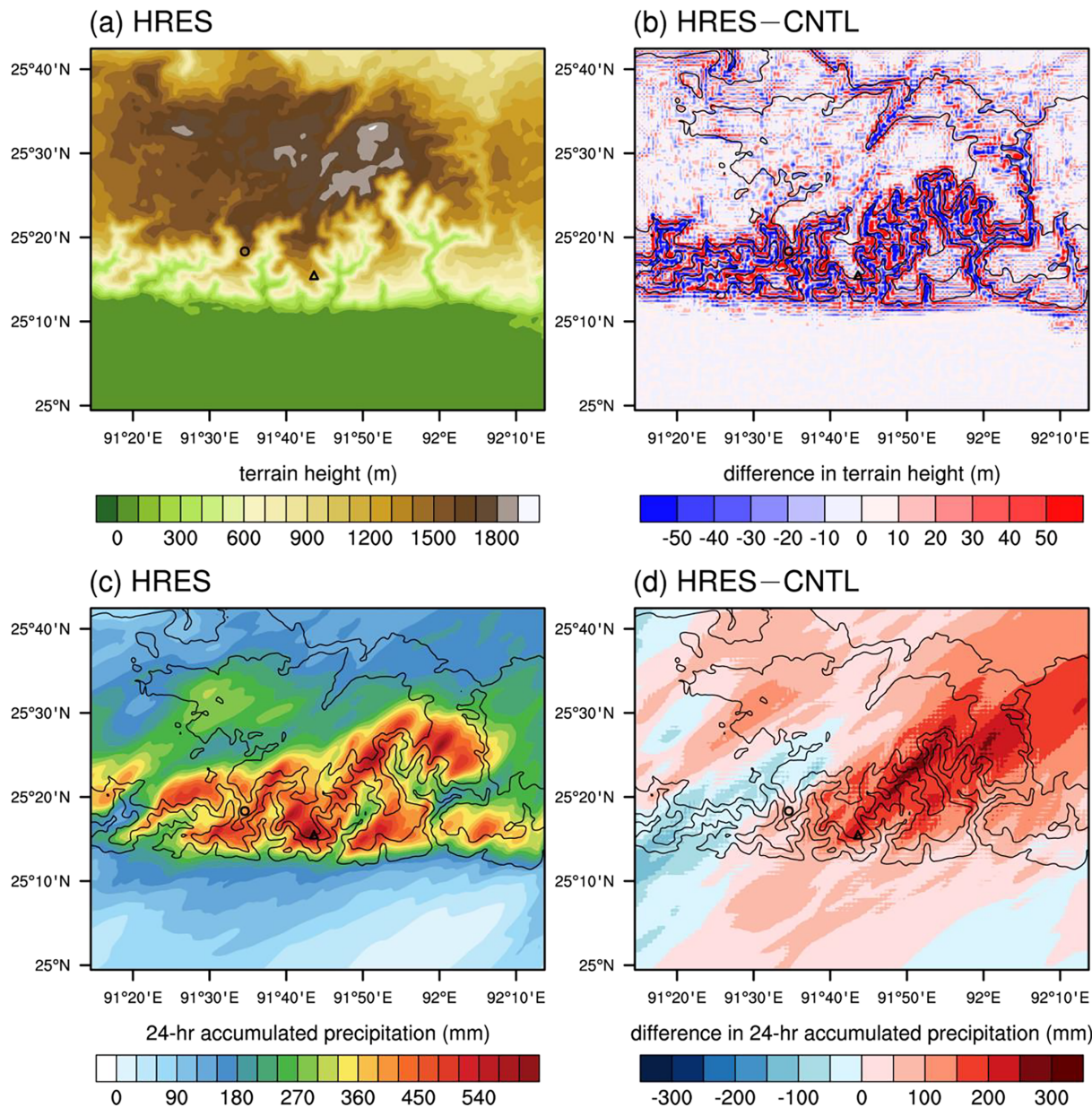


FIGURE 15 (a) Terrain height in the HRES simulation and (b) the difference between the HRES and CNTL simulations. (c) Twenty-four hr accumulated precipitation amount in the HRES simulation and (d) the difference between the HRES and CNTL simulations. Terrain height is contoured at 400 m intervals in (b–d) [Colour figure can be viewed at wileyonlinelibrary.com]

HRES simulation are 472, 364 and 521 mm, respectively, for Cherrapunji, and 745, 270 and 350 mm, respectively, for Mawsynram. The largest increase is seen along the steep slope northeast of Cherrapunji where the difference in terrain height is large. This implies that the steepness of the terrain largely affects the precipitation intensity.

The steeper slope can intensify orographic updraughts and downdraughts. The intensified orographic flows may be a cause of the increased precipitation in the HRES simulation. Figure 16 shows the vertical velocity at $z = 3$ km averaged over P2. Note that the vertical velocity at $z = 3$ km in P1 does not show significant differences between the

HRES and CNTL simulations (not shown). The overall spatial patterns look similar in both simulations. The updraughts appear over the upslope area of valleys, while the downdraughts appear over the downslope area of valleys in both simulations. However, there are differences in the magnitude of vertical velocities between the two simulations. The contoured frequency by altitude diagrams (CFADs) of vertical velocity show that strong updraughts are more frequent and the weak vertical velocities less than $1 \text{ m} \cdot \text{s}^{-1}$ are less frequent in the HRES simulation (Figure 17). This means that the variability of vertical velocity is high in the HRES simulation. In the spatial

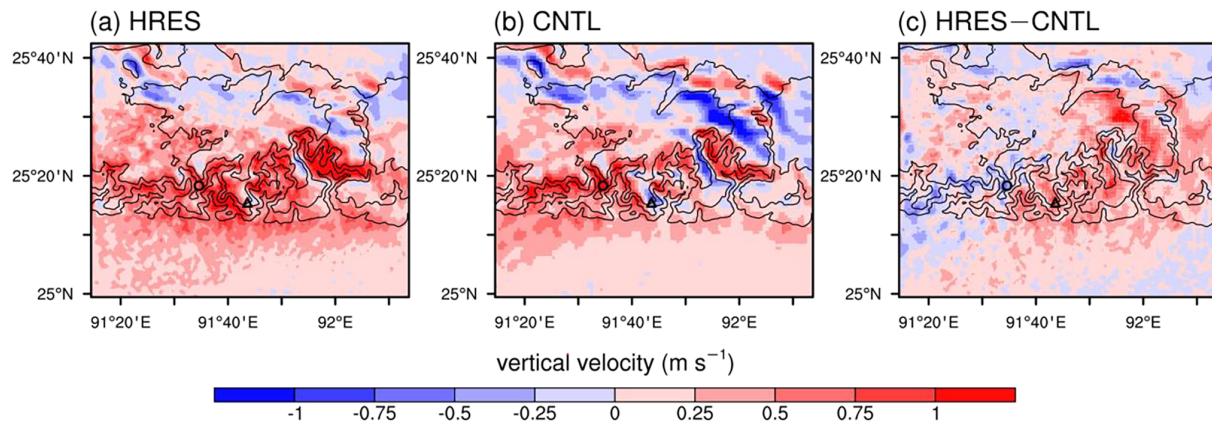


FIGURE 16 Horizontal distributions of vertical velocity at $z = 3$ km averaged over P2 (0000–0900 LST 19 August 2015) in the (a) HRES and (b) CNTL simulations, and (c) their difference. Terrain height is contoured at 400 m intervals [Colour figure can be viewed at [wileyonlinelibrary.com](#)]

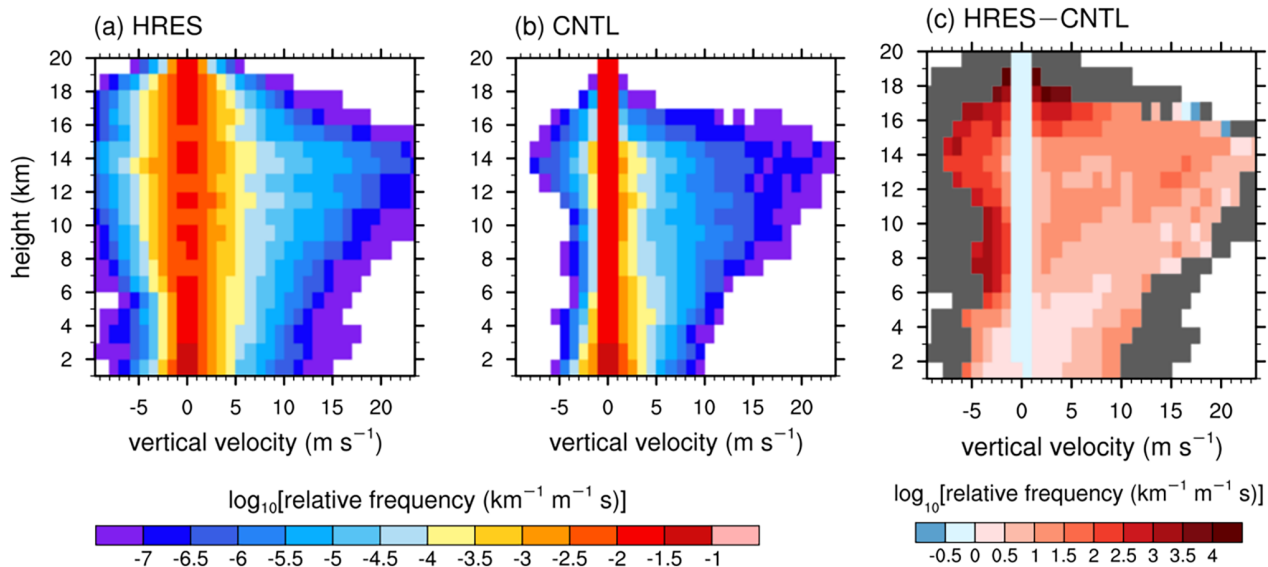


FIGURE 17 Contoured frequency by altitude diagrams (CFADs) of vertical velocity in the (a) HRES and (b) CNTL simulations, and (c) their difference. Bins with HRES values but without CNTL values are indicated by grey colour in (c) [Colour figure can be viewed at [wileyonlinelibrary.com](#)]

distribution (Figure 16), only the updraughts are intensified, while the downdraughts are weakened. This results in an overall increase in vertical velocity around Cherrapunji. The regions with the overall increase in vertical velocity are well-matched with the regions with increased precipitation (Figures 15d and 16c). This implies that the enhanced vertical velocity by steeper slopes in the HRES simulation is closely related to the increased precipitation.

4 | SUMMARY AND CONCLUSIONS

In this study, dynamical, thermodynamical and cloud microphysical characteristics associated with the 18–19

August 2015 extremely heavy precipitation case in the MP region are examined through high-resolution WRF model simulations. Three simulations (CNTL, noMP and HRES) are performed. The results of the CNTL and noMP simulations show that MP both initiates and intensifies precipitation. When LLJ and water vapour transport are weak (P1), the orographic lifting induced by MP initiates precipitation. Liquid hydrometeors and the associated warm cloud microphysical processes are dominant. The accretion process mainly contributes to the heavy precipitation in P1. When LLJ and water vapour transport are strong (P2), a number of deep convective systems are developed upwind of MP. These convective systems merge and intensify in the upslope region. The stronger

updraughts in P2 than in P1 result in the larger accretion rate which is the main contributor to the heavy precipitation in the upslope region. The melting of ice hydrometeors also contributes to the precipitation in P2. The local topographic effects on the extreme precipitation are investigated by comparing the results of the HRES simulation to those of the CNTL simulation. The increase in horizontal resolution makes the southern slope of MP steeper, resulting in intensified updraughts and weakened downdraughts. The region with increased vertical velocity (northeast of Cherrapunji) is well-matched with the region with increased precipitation. The increase in simulated precipitation in the HRES simulation reduces the deviation from the rain-gauge observation seen in the CNTL simulation, implying the importance of very high horizontal resolutions in the simulations of extremely heavy precipitation in MP.

The precipitation case selected in this study is one of the most extreme precipitation cases in the MP region in recent years. It is worth investigating whether the dynamical, thermodynamical and cloud microphysical characteristics of the extreme precipitation case in this study are general characteristics of monsoonal precipitation in the MP region. For this, numerical modelling studies of various monsoonal precipitation cases in this region are needed. The simulation of the extremely heavy precipitation event in this study was found to be sensitive to the choice of physics parametrization schemes although this feature is not shown in this study. A future systematic investigation on the sensitivities of this simulation to different physics parametrization schemes is expected to help understanding and prediction of extremely heavy precipitation in which orographic forcing plays an important role.

ACKNOWLEDGEMENTS

This work was supported by the National Research Foundation of Korea (NRF-2019R1A6A1A10073437). We thank two anonymous reviewers for providing valuable comments.

AUTHOR CONTRIBUTIONS

Tanvir Ahmed: Formal analysis; investigation; validation; visualization; writing – original draft. **Joohyun Lee:** Formal analysis; investigation; validation; visualization; writing – original draft. **Han-Gyul Jin:** Formal analysis; writing – original draft; writing – review and editing. **Jong-Jin Baik:** Conceptualization; formal analysis; supervision; writing – review and editing.

CONFLICT OF INTEREST

The authors declare no conflict of interest.

ORCID

Han-Gyul Jin  <https://orcid.org/0000-0001-5618-3529>
Jong-Jin Baik  <https://orcid.org/0000-0003-3709-0532>

REFERENCES

- Ahmed, T., Jin, H.-G. and Baik, J.-J. (2020a) Spatiotemporal variations of precipitation in Bangladesh revealed by nationwide rain gauge data. *Asia-Pacific Journal of Atmospheric Sciences*, 56, 593–602.
- Ahmed, T., Jin, H.-G. and Baik, J.-J. (2020b) A physically based raindrop–cloud droplet accretion parametrization for use in bulk microphysics schemes. *Quarterly Journal of the Royal Meteorological Society*, 146, 3368–3383.
- Blackadar, A.K. (1957) Boundary layer wind maxima and their significance for the growth of nocturnal inversions. *Bulletin of the American Meteorological Society*, 38, 283–290.
- Choudhury, B.A., Saha, S.K., Konwar, M., Sujith, K. and Deshamukhya, A. (2019) Rapid drying of northeast India in the last three decades: climate change or natural variability? *Journal of Geophysical Research: Atmospheres*, 124, 227–237.
- Danielson, J.J. and Gesch, D.B. (2011) *Global multi-resolution terrain elevation data 2010 (GMTED2010)*. US Geological Survey Open-File Report 2011-1073, 26 pp.
- Dudhia, J. (1989) Numerical study of convection observed during the Winter Monsoon Experiment using a mesoscale two-dimensional model. *Journal of the Atmospheric Sciences*, 46, 3077–3107.
- Farr, T.G., Rosen, P.A., Caro, E., Crippen, R., Duren, R., Hensley, S., Kobrick, M., Paller, M., Rodriguez, E., Roth, L., Seal, D., Shaffer, S., Shimada, J., Umland, J., Werner, M., Oskin, M., Burbank, D. and Alsdorf, D. (2007) The shuttle radar topography mission. *Reviews of Geophysics*, 45, RG2004.
- Fujinami, H., Hatsuzuka, D., Yasunari, T., Hayashi, T., Terao, T., Murata, F., Kiguchi, M., Yamane, Y., Matsumoto, J., Islam, M.N. and Habib, A. (2011) Characteristic intraseasonal oscillation of rainfall and its effect on interannual variability over Bangladesh during boreal summer. *International Journal of Climatology*, 31, 1192–1204.
- Fujinami, H., Sato, T., Kanamori, H. and Murata, F. (2017) Contrasting features of monsoon precipitation around the Meghalaya Plateau under westerly and easterly regimes. *Journal of Geophysical Research: Atmospheres*, 122, 9591–9610.
- Goswami, B.B., Mukhopadhyay, P., Mahanta, R. and Goswami, B.N. (2010) Multiscale interaction with topography and extreme rainfall events in the northeast Indian region. *Journal of Geophysical Research*, 115, D12114.
- Habib, S.M.A., Sato, T. and Hatsuzuka, D. (2019) Decreasing number of propagating mesoscale convective systems in Bangladesh and surrounding area during 1998–2015. *Atmospheric Science Letters*, 20, e879.
- Hersbach, H., Bell, B., Berrisford, P., Hirahara, S., Horányi, A., Muñoz-Sabater, J., Nicolas, J., Peubey, C., Radu, R., Schepers, D., Simmons, A., Soci, C., Abdalla, S., Abellán, X., Balsamo, G., Bechtold, P., Biavati, G., Bidlot, J., Bonavita, M., Chiara, G., Dahlgren, P., Dee, D., Diamantakis, M., Dragani, R., Flemming, J., Forbes, R., Fuentes, M., Geer, A., Haimberger, L., Healy, S., Hogan, R.J., Hölm, E., Janisková, M., Keeley, S., Laloyaux, P., Lopez, P., Lupu, C., Radnoti, G., Rosnay, P., Rozum, I., Vamborg, F., Villaume, S. and Thépaut, J.-N. (2020) The ERA5 global reanalysis. *Quarterly Journal of the Royal Meteorological Society*, 146, 1999–2049.

- Hong, S.-Y., Noh, Y. and Dudhia, J. (2006) A new vertical diffusion package with an explicit treatment of entrainment processes. *Monthly Weather Review*, 134, 2318–2341.
- Islam, M.N., Terao, T., Uyeda, H., Hayashi, T. and Kikuchi, K. (2005) Spatial and temporal variations of precipitation in and around Bangladesh. *Journal of the Meteorological Society of Japan*, 83, 21–39.
- Jiang, X., Lau, N.-C., Held, I.M. and Ploshay, J.J. (2007) Mechanisms of the Great Plains low-level jet as simulated in an AGCM. *Journal of the Atmospheric Sciences*, 64, 532–547.
- Kain, J.S. (2004) The Kain–Fritsch convective parameterization: an update. *Journal of Applied Meteorology*, 43, 170–181.
- Kataoka, A. and Satomura, T. (2005) Numerical simulation on the diurnal variation of precipitation over northeastern Bangladesh: a case study of an active period 14–21 June 1995. *SOLA*, 1, 205–208.
- Kuttippurath, J., Murasingh, S., Stott, P.A., Sarojini, B.B., Jha, M.K., Kumar, P., Nair, P.J., Varikoden, H., Raj, S., Francis, P.A. and Pandey, P.C. (2021) Observed rainfall changes in the past century (1901–2019) over the wettest place on Earth. *Environmental Research Letters*, 16, 024018.
- Lee, H. and Baik, J.-J. (2017) A physically based autoconversion parameterization. *Journal of the Atmospheric Sciences*, 74, 1599–1616.
- Mlawer, E.J., Taubman, S.J., Brown, P.D., Iacono, M.J. and Clough, S.A. (1997) Radiative transfer for inhomogeneous atmospheres: RRTM, a validated correlated-k model for the longwave. *Journal of Geophysical Research*, 102, 16663–16682.
- Murata, F., Terao, T., Hayashi, T., Asada, H. and Matsumoto, J. (2008) Relationship between atmospheric conditions at Dhaka, Bangladesh, and rainfall at Cherrapunjee, India. *Natural Hazards*, 44, 399–410.
- Murata, F., Terao, T., Fujinami, H., Hayashi, T., Asada, H., Matsumoto, J. and Syiemlieh, H.J. (2017) Dominant synoptic disturbance in the extreme rainfall at Cherrapunji, northeast India, based on 104 years of rainfall data (1902–2005). *Journal of Climate*, 30, 8237–8251.
- Ohsawa, T., Ueda, H., Hayashi, T., Watanabe, A. and Matsumoto, J. (2001) Diurnal variations of convective activity and rainfall in tropical Asia. *Journal of the Meteorological Society of Japan*, 79, 333–352.
- Orr, A., Listowski, C., Couttet, M., Collier, E., Immerzeel, W., Deb, P. and Bannister, D. (2017) Sensitivity of simulated summer monsoonal precipitation in Langtang Valley, Himalaya, to cloud microphysics schemes in WRF. *Journal of Geophysical Research: Atmospheres*, 122, 6298–6318.
- Sato, T. (2013) Mechanism of orographic precipitation around the Meghalaya Plateau associated with intraseasonal oscillation and the diurnal cycle. *Monthly Weather Review*, 141, 2451–2466.
- Skamarock, W.C., Klemp, J.B., Dudhia, J., Gill, D.O., Liu, Z., Berner, J., Wang, W., Powers, J.G., Duda, M.G., Barker, D.M. and Huang, X.-Y. (2019) *A description of the Advanced Research WRF model version 4*. NCAR Technical Note NCAR/TN-475+STR. Boulder, CO: National Center for Atmospheric Research.
- Terao, T., Islam, M.N., Hayashi, T. and Oka, T. (2006) Nocturnal jet and its effects on early morning rainfall peak over northeastern Bangladesh during the summer monsoon season. *Geophysical Research Letters*, 33, 3–7.
- Tewari, M., Chen, F., Wang, W., Dudhia, J., LeMone, M.A., Mitchell, K., Ek, M., Gayno, G., Wegiel, J. and Cuenca, R.H. (2004) Implementation and verification of the unified NOAH land surface model in the WRF model. In: *20th Conference on Weather Analysis and Forecasting/16th Conference on Numerical Weather Prediction*, 12–16 January 2004. Seattle, WA: American Meteorological Society.
- Thompson, G. and Eidhammer, T. (2014) A study of aerosol impacts on clouds and precipitation development in a large winter cyclone. *Journal of the Atmospheric Sciences*, 71, 3636–3658.
- Varikoden, H. and Revadekar, J.V. (2020) On the extreme rainfall events during the southwest monsoon season in northeast regions of the Indian subcontinent. *Meteorological Applications*, 27, e1822.
- Wang, Z. and Chang, C.-P. (2012) A numerical study of the interaction between the large-scale monsoon circulation and orographic precipitation over South and Southeast Asia. *Journal of Climate*, 25, 2440–2455.
- Wu, C.-H., Hsu, H.-H. and Chou, M.-D. (2014) Effect of the Arakan Mountains in the northwestern Indochina Peninsula on the late May Asian monsoon transition. *Journal of Geophysical Research: Atmospheres*, 119, 10769–10779.

How to cite this article: Ahmed, T., Lee, J., Jin, H.-G. & Baik, J.-J. (2022) Processes associated with extremely heavy precipitation in the Meghalaya Plateau region: A case modelling study. *Quarterly Journal of the Royal Meteorological Society*, 148(744), 1057–1074. Available from: <https://doi.org/10.1002/qj.4246>